

Article

# The Average Grain Size and Grain Aspect Ratio in Metal Laser Powder Bed Fusion: Modeling and Experiment

Morgan Letenneur, Alena Kreitchberg and Vladimir Brailovski \* 

Department of Mechanical Engineering, École de technologie supérieure, 1100 Notre-Dame Street West, Montreal, QC H3C 1K3, Canada; morgan.letenneur.1@etsmtl.net (M.L.); alena.kreitchberg.1@ens.etsmtl.ca (A.K.)

\* Correspondence: vladimir.brailovski@etsmtl.ca; Tel.: +1-514-396-8594

Received: 31 January 2020; Accepted: 8 March 2020; Published: 11 March 2020



**Abstract:** The additive manufacturing (AM) process induces high uncertainty in the mechanical properties of 3D-printed parts, which represents one of the main barriers for a wider AM processes adoption. To address this problem, a new time-efficient microstructure prediction algorithm was proposed in this study for the laser powder bed fusion (LPBF) process. Based on a combination of the melt pool modeling and the design of experiment approaches, this algorithm was used to predict the microstructure (grain size/aspect ratio) of materials processed by an EOS M280 LPBF system, including Iron and IN625 alloys. This approach was successfully validated using experimental and literature data, thus demonstrating its potential efficiency for the optimization of different LPBF powders and systems.

**Keywords:** additive manufacturing; laser powder bed fusion; process optimization; analytical model; microstructure

## 1. Introduction

The additive manufacturing (AM) process is “the process of joining materials to make objects from 3D computer-aided design (CAD) model data, usually layer upon layer, as opposed to subtractive manufacturing technologies” [1]. Currently, most AM systems belong to the laser powder bed fusion system (LPBF) category. In this process, the laser executes a specific journey defined by the laser power and speed, the distance between tracks (hatching space), and the layer thickness to build a part. This multi-tracking strategy results in the complex thermal history and specific anisotropic microstructure of 3D-printed parts [2–4]. This specificity of the final microstructure with a resulting uncertainty in the mechanical properties of 3D-printed parts, has been found to be the main barrier to a wider AM process adoption [5]. Since it is not possible to experimentally analyze all parts manufactured by AM, numerical simulations represent an appealing time- and resource-saving approach to predict the parts’ microstructure [6]. Given the complexity of the LPBF process, which involves around 130 printing variables [7], high-fidelity melt pool models are, however, very complex and require delicate calibration procedures. Ideally, such models must take into account the transient non-equilibrium physical phenomena involved in the processes such as the heat flow, the Marangoni effect, keyhole mode melting and gravity forces [8–12].

Moreover, to predict the as-printed material microstructure, results of such melt pool simulations must be coupled with microstructure simulation models, such as the phase-field model, for example [13–16]. In addition to involving huge computing resources, these models can only predict the microstructure in the melt pool, and do not take into account local melting-remelting phenomena and heterogeneous non-stationary temperature fields in 3D-printed parts, although both aspects

affect the parts' final microstructure [17]. Furthermore, during the manufacturing of a part, the multi-track pattern introduces variable defects such as micro-porosity, liquation cracks, microstructural heterogeneity and segregation, which will also influence the final microstructure [18–21]. Modeling all these phenomena at once represents an issue that remains unresolved.

Notwithstanding the above, since the as-printed material microstructure (grain and subgrain size and distribution, crystallographic texture and phases) determines the level of mechanical properties, different models have been developed to fill the gap between the processing conditions and the printed parts' microstructure, with varying degrees of success. Most of these models are based on mass, momentum and energy conservation principles [4,22–24] and among them, the heat conduction and thermal-fluid models are the most commonly used [24]. The heat conduction simulations are computationally efficient, but they do not take into account the phase changes between the solid and liquid states occurring during powder melting/remelting. These models can either be simple and only consider the thermal exchanges between the laser and the powder bed, or more complex, taking into consideration the multiple effects seen during LPBF, such as the keyholing and the balling effects [12] or the Marangoni effect [24]. Less commonly, thermal fluid vaporization models are also utilized in order to take into account heat losses caused by vaporization [12,24]. While all these modeling approaches are well suited for melt pool simulations, they are, however, barely suitable for full part computations or for printing parameters optimization, since they are very computing resources-consuming.

To circumvent the above problem and facilitate the adoption of new LPBF alloys, a simplified approach, allowing the simulation of thousands of printing parameter sets in a very time-efficient way, was developed and validated in our previous work [25–27]. In the present study, we consider the microstructure of LPBF manufactured parts to be mostly dependent on the cooling rate (CR) and the thermal gradient (TG) in the vicinity of the melt pool [24,28]. Based on this assertion, we focus here on the possibility of using these two metrics to correlate a specific combination of LPBF processing parameters (laser power, scanning speed, layer thickness, and hatching space) with the grain size and grain aspect ratio of a printed material.

## 2. Methodology

This study was conducted in three phases: first, an analytical model of the thermal field generated by a moving heat source in a solid body was used to evaluate the melt pool solidification cooling rate (CR) and the thermal gradient (TG) for a given set of LPBF processing parameters, namely the laser power, scanning speed, layer thickness, and hatching space. Next, to calibrate the model for a given material and a given LPBF system, the relationships between CR and TG and the grain size ( $d$ ) and the grain aspect ratio (GAR) of the printed material were found experimentally. Finally, using the numerical model developed and the experimental relationships found, the LPBF processing parameters were directly linked to the microstructure of the specimens manufactured using the selected LPBF system, with the ultimate objective of developing a generic grain size and grain aspect ratio prediction algorithm for different materials and different LPBF systems.

### 2.1. Cooling Rate (CR) and Thermal Gradient (TG) Calculations

The LPBF melt pool temperature distribution calculations were carried out using the analytical model of a semi-infinite solid with a moving Gaussian heat source [29]. This model has been successfully used for density prediction in specimens manufactured from Fe [25], Ti-Zr-Nb [26], AlSiMg, IN625, Ti64 and 316L alloy powders [27]. The Gaussian model involves a symmetrical distribution of laser irradiance across the beam. The energy from the laser is assumed to be applied on the powder bed surface for a time interval defined by the scanning speed and the laser spot size. In this case, for a Gaussian beam moving with a given velocity, the temperature distribution  $T(x, y, z)$  in the powder bed is calculated by Equations (1)–(3):

$$T(x,y,z) = T_0 + \frac{AP}{kr_f\pi^{\frac{3}{2}}} \int_{\infty}^0 \frac{1}{1+\tau^2} \exp(C) d\tau \tag{1}$$

$$C = -\frac{\tau^2}{1+\tau^2} \left[ \left( \xi - \frac{Pe}{2\tau^2} \right)^2 + \eta^2 \right] - \tau^2 \zeta^2 \tag{2}$$

$$\xi = \sqrt{2} \frac{x}{r_f}, \eta = \sqrt{2} \frac{y}{r_f}, \zeta = \sqrt{2} \frac{z}{r_f}, Pe = \frac{r_f v}{2\sqrt{2}\alpha}, \tau = \frac{r_f}{2\sqrt{2}\alpha t}, \alpha = \frac{k}{\rho \times C_p} \tag{3}$$

where  $T_0$  is the powder bed temperature (°C);  $A$ , the absorptivity;  $P$ , the laser power (W);  $k$ , the thermal conductivity (W/m·K);  $r_f$ , the laser beam radius (m);  $Pe$ , the Peclet number;  $v$ , the scanning speed (m/s);  $\alpha$ , the thermal diffusivity (m<sup>2</sup>/s);  $\rho$ , the irradiated material density (kg/m<sup>3</sup>);  $C_p$ , the specific heat (J/kg·K), and  $t$ , the time (s).

The laser energy absorptivity  $A$  is estimated using Equation (4) [30]:

$$A \approx 0.365(\lambda\sigma)^{-0.5} = 0.365\left(\frac{R}{\lambda}\right)^{0.5} \tag{4}$$

where  $\lambda$  is the laser wavelength (μm),  $\sigma$ , the electrical conductivity (S/m), and  $R$ , the electrical resistivity of the irradiated material (Ω·m).

Then, based on previous studies on additive manufacturing and welding [24,31], the solidification cooling rate (CR) and the thermal gradient (TG) are calculated along the direction of the meltpool in the region encompassed between the liquidus and solidus temperatures (Equations (5) [24] and (6) and Figure 1):

$$\text{Cooling rate (CR)} = \frac{dT}{dt} = \frac{T_{liq} - T_{sol}}{(d_{liq} - d_{sol}) \times v} \tag{5}$$

$$\text{Thermal gradient (TG)} = \frac{\partial T(x, 0, 0)}{\partial x} \tag{6}$$

where  $T_{liq}$  is the liquidus temperature;  $T_{sol}$ , the solidus temperature;  $d_{liq}$ , the position along the centerline of the track where the temperature is equal to  $T_{liq}$ ;  $d_{sol}$ , the position along the centerline of the track where the temperature is equal to  $T_{sol}$ ; and  $v$  is the speed of the laser.

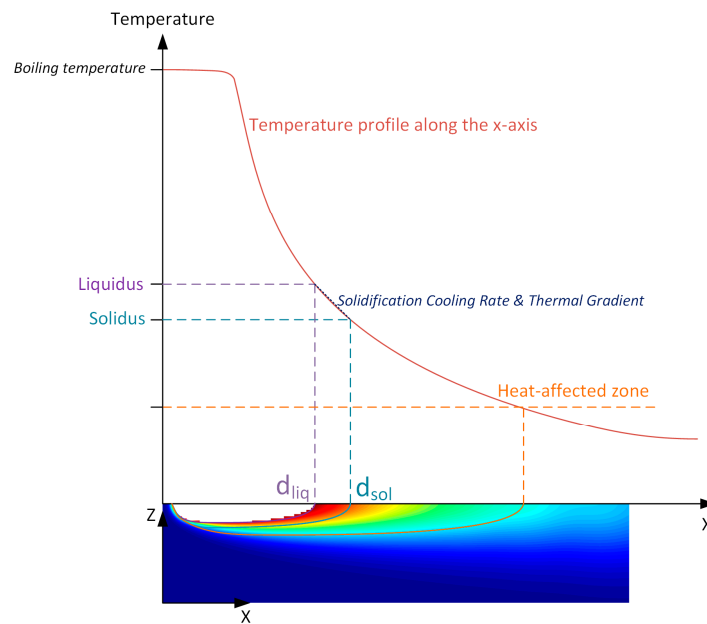


Figure 1. Schematized temperature profile along meltpool centerline.

## 2.2. Experimental Calibration of the Melt Pool Model

### 2.2.1. Materials, Equipment and Plan of Experiment

The experimental part of this study was conducted using water-atomized iron powder (RTMP, Sorel-Tracy, Canada) of the following composition (weight %): Fe: bal., Mn: 0.04, C: 0.004, O: 0.08, S: 0.007, and N: 0.004. The process of water atomization results in relatively coarse and irregular powder particles with a particle size distribution of  $D_{10,3} = 15.2 \mu\text{m}$ ,  $D_{50,3} = 29.1 \mu\text{m}$ ,  $D_{90,3} = 50.7 \mu\text{m}$  (Figure 2a) and a mean sphericity of 0.67 (Figure 2b). The powder batch chemistry was analyzed as follows: Fe and Mn, using a Spectro ARL 3460 system (ThermoFisher Scientific, Waltham, MA, USA) (ASTM E-415); O, N and C, S using LECO TC436DC and LECO CS844 systems respectively (Leco, St Joseph, MI, USA) (ASTM E-1019). The powder PSD was measured using a Master Sizer 3000 (Malvern Panalytical, Malvern, UK) laser diffraction particle size analyzer and calculated following the ISO 9276 standard. The powder sphericity was calculated using the following formula:

$$S = \frac{4 \times \pi \times A}{P^2} \tag{7}$$

where  $A$  and  $P$  are the area and the perimeter of iron powder particles calculated from the images obtained by scanning electron microscopy.

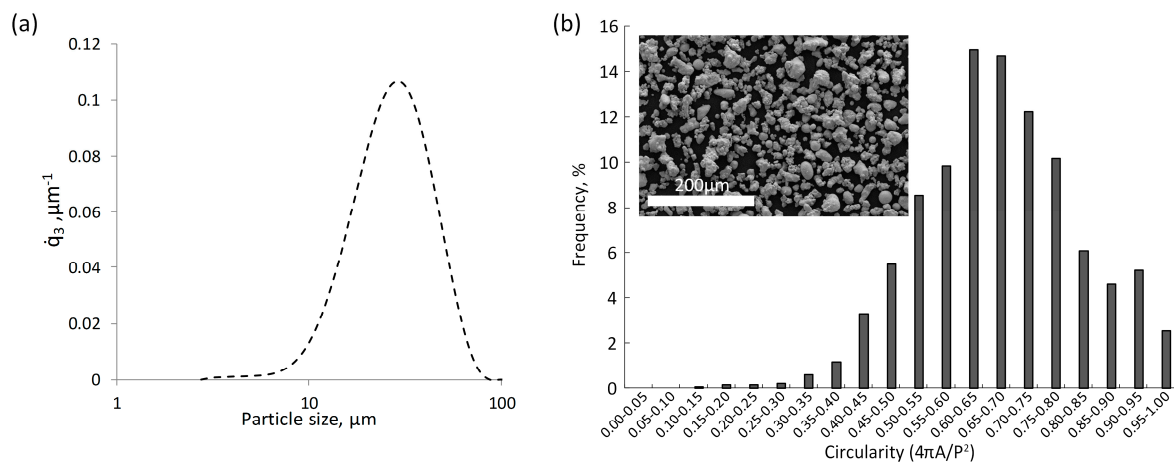


**Figure 2.** Water-atomized iron powder: (a) particles size distribution (b) circularity distribution and typical scanning electron microscope (SEM) image.

This powder was processed using an EOSINT M280 LPBF system (EOS GmbH, Munich, Germany) equipped with a 400 W ytterbium fiber laser (effective beam radius  $r_f = 40 \mu\text{m}$  provided by EOS) and a standard EOS ceramic doctor blade.

To design the plan of the experiments, the analytical model represented by Equations (1)–(4) is used first. To provide input values for this model, the physical properties of an irradiated powder, namely the thermal conductivity  $k$  [32], the electrical resistivity  $R$  [33] and the powdered material density  $\rho$  are calculated as follows:

$$k = k_0 \times \frac{\phi}{0.5 \times (3 - \phi)}; R = 0.696 \times \frac{4}{\phi} \times R_0; \rho = \phi \times \rho_0 \tag{8}$$

In this work, the effective RTMP powder bed density  $\phi$ , which is dependent on the powder size distribution and morphology, and the characteristics of a spreading mechanism, was measured using the encapsulated samples method [34] and was found to be close to 40%. The bulk and powder properties used for calculations are given in Table 1 [35,36]. Given the lack of experimental values for the thermal conductivity and specific heat of RTMP iron powders, the corresponding values for a

similar AISI 1008 alloy were applied [35]. The initial temperature of the substrate (building platform) was considered to be 23 °C and it was assumed that the preceding layer cools down to the initial temperature between two neighboring scanning tracks.

**Table 1.** Physical properties of an AISI 1008 alloy [35,36].

Properties	Bulk	Powder ( $\varphi = 40\%$ )
Liquidus temperature, °C	1535	1535
Solidus temperature, °C	1494	1494
Density, kg/m <sup>3</sup>	7860	3144
Thermal conductivity, W/m × K	81	25
Specific heat capacity, J/kg × K	469	469
Electrical resistivity, 10 <sup>-8</sup> Ω × m	8.9	62

The temperature distribution map shown in Figure 3 represents an example of the single track calculations using Equations (1)–(4) and (8). It has the following set of LPBF processing parameters:  $P = 270\text{ W}$ ,  $v = 1500\text{ mm/s}$ , and  $t = 40\text{ }\mu\text{m}$  applied to iron powder (Table 1). From this temperature map, the solidification cooling rate and the thermal gradient were calculated along the center line using Equations (5) and (6) corresponding to  $1.43 \times 10^7\text{ }^\circ\text{C/s}$  and  $9.54 \times 10^6\text{ }^\circ\text{C/mm}$ , respectively.

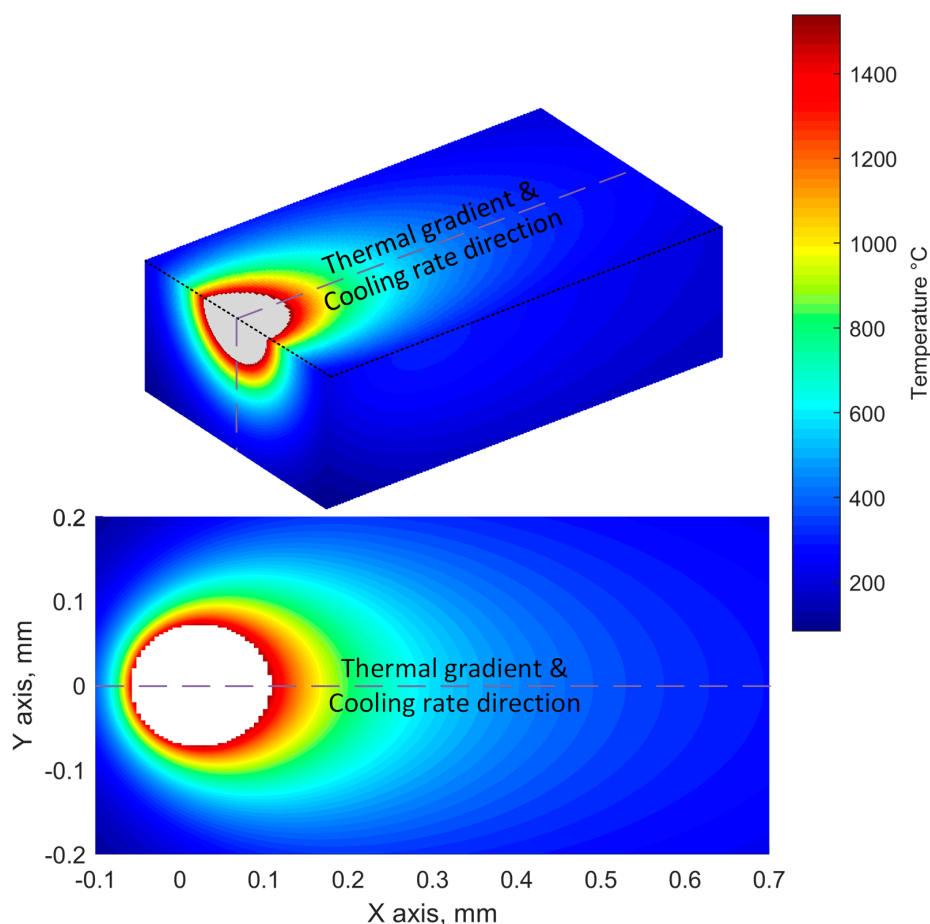


**Figure 3.** Calculated melt pool for iron powder when  $P = 270\text{ W}$ ,  $v = 1500\text{ mm/s}$ , and  $t = 40\text{ }\mu\text{m}$ .

### 2.2.2. Solidification Cooling Rate and Thermal Gradient—Microstructure Relationship

Firstly, to establish the relationship between the LPBF processing parameters and the printed material density, the algorithm developed in [27] was used to build a so-called “density processing

map” (Figure 4a) in the laser energy density ( $E$ , J/mm<sup>3</sup>) (Equation (9))—material build rate ( $BR$ , cm<sup>3</sup>/h) (Equation (10)) coordinates:

$$E(\text{J/mm}^3) = \frac{P}{v \times h \times t} \tag{9}$$

$$BR(\text{cm}^3/\text{h}) = v \times h \times t \tag{10}$$

where  $P$  is the laser power ranging from 40 to 380 W;  $v$ , the laser speed ranging from 200 to 4000 mm/s;  $h$ , the hatching space ranging from 60 to 200 μm; and the constant layer thickness of  $t = 40$  μm. For the next step of this study, the narrower range of the E-BR processing conditions corresponding to a density of the printed material  $\geq 99.9\%$  was isolated as shown in Figure 4b.

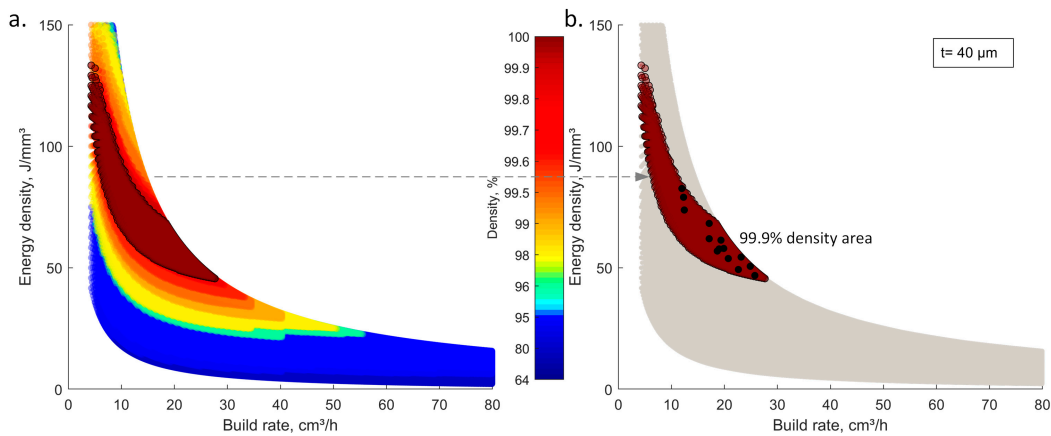


**Figure 4.** Density processing map for iron: powder (a) all densities (b)  $\geq 99.9\%$  density area; dots identify 14 processing condition sets used for model calibration (see further).

Next, using Equations (5) and (6), the CR and TG processing maps for iron powder can be computed (Figure 5a,b). It can be noted from these maps that for a printed density  $\geq 99.9\%$ , the cooling rate ranges from  $1.5$  to  $3.4 \times 10^7$  °C/s, and the thermal gradient from  $1.1$  to  $1.4 \times 10^7$  °C/mm. Finally, for the model validation, 14 sets of printed conditions are randomly distributed in the  $\geq 99.9\%$  density zone (see dots in Figures 4b and 5a,b), and the corresponding printing parameters  $P$ ,  $v$  and  $h$  reverse-calculated using the set of Equations (1)–(4), and reported in Table 2.

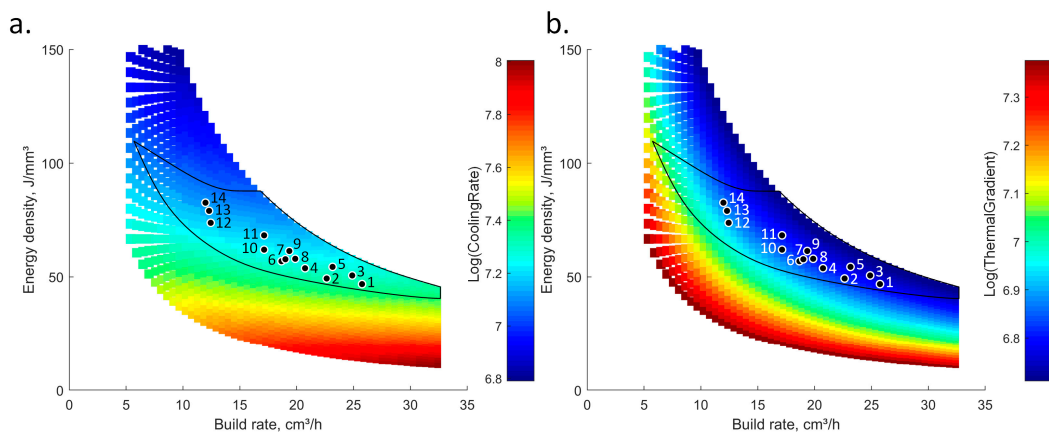


**Figure 5.** (a) Cooling rate and (b) thermal gradient processing maps for iron powder; contours delimit the processing conditions corresponding to a printed density  $\geq 99.9\%$ ; dots identify 14 printing condition sets used for model calibration.

**Table 2.** Printing parameters ( $t = 40 \mu\text{m}$ ) and calculated BR, E, Printed density, CR and TG.

#	$P, W$	$v, \text{m/s}$	$h, \text{mm}$	BR, $\text{cm}^3/\text{h}$	$E, \text{J}/\text{mm}^3$	Printed Density, %	CR, $10^7 \text{ }^\circ\text{C/s}$	TG, $10^7 \text{ }^\circ\text{C}/\text{mm}$
1	255	0.96	0.09	12.4	73.8	100	1.46	1.53
2	270	1.22	0.07	12.3	79.0	99.9	1.74	1.43
3	275	1.04	0.08	12.0	82.6	99.9	1.46	1.40
4	295	1.62	0.08	18.7	56.9	99.9	2.11	1.30
5	295	1.7	0.07	17.1	62.0	100	2.21	1.30
6	305	2.2	0.06	19.0	57.8	99.9	2.76	1.26
7	310	2.62	0.06	22.6	49.3	99.9	3.22	1.23
8	310	2.4	0.06	20.7	53.8	99.9	2.96	1.23
9	320	2.3	0.06	19.9	58.0	99.9	2.75	1.19
10	325	1.7	0.07	17.1	68.3	99.9	2.00	1.18
11	330	1.92	0.07	19.4	61.4	100	2.23	1.16
12	335	2.98	0.06	25.7	46.8	99.9	3.40	1.14
13	350	2.88	0.06	24.9	50.6	99.9	3.14	1.09
14	350	2.68	0.06	23.2	54.4	99.9	2.93	1.10

For each set of printing parameters, three  $10 \times 10 \times 20$  (mm) parallelepiped specimens were printed (Figure 6), cut off the building plate and polished, and their densities were measured using the Archimedes technique (ASTM B962-15) with a SARTORIUS Secura 324-1s scale (Sartorius, Goettingen, Germany), having a precision of  $\sim 0.001$  g. Each density measurement was repeated at least 3 times.

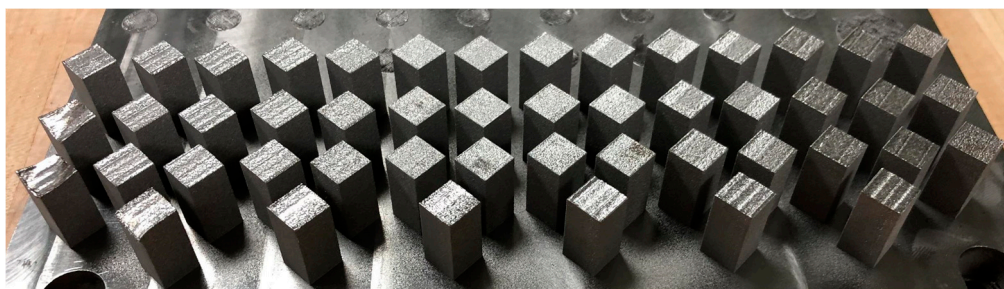


**Figure 6.** Build plate with iron specimens.

Then, for grain size and grain aspect ratio measurements, the specimens were cross-sectioned in the XY and XZ directions, mounted in bakelite, manually polished and attacked with a nital solution. The vertical (parallel to the build direction, Plan XZ) and horizontal (perpendicular to the build direction, Plan XY) faces of the specimens were analyzed using a LEXT4100 confocal microscope (Olympus, Tokyo, Japan) with an  $\times 500$  magnification and then processed using Matlab software (see typical metallography image in Figure 7). The average grain size in the XZ ( $d_{xz}$ ) and XY ( $d_{xy}$ ) plans was measured using the linear intercept method [37], and the grain aspect ratios  $\text{GAR} = d_{xz}/d_{xy}$  were calculated. These data are plotted as functions of the CR & TG in Figure 8a,b for all 14 sets of printed parameters.

In Figure 8b, it can be stated that the higher the cooling rate, the lower both the grain size and the grain aspect ratio of printed specimens, and vice versa. On the contrary, the greater the thermal gradient, the larger the grain size and the aspect ratio; the second trend here is much less pronounced than the first. Assuming that the calculated CR&TG values correspond to the effectively obtained melt pool characteristics, the grain size and the grain aspect ratio values can now be expressed as their functions using the linear least square method:

$$d_{xz} \text{ or GAR} = a_0 + a_1 \times \left(\frac{\text{CR}}{10^7}\right)^{a_2} + a_3 \times \left(\frac{\text{TG}}{10^7}\right)^{a_4} \tag{11}$$

where  $a_0 = 12.4$ ,  $a_1 = 34.65$ ,  $a_2 = -3.265$ ,  $a_3 = 0.0003$  and  $a_4 = 24.11$  for the grain size ( $dxz$ ), and  $a_0 = 15.5$ ,  $a_1 = -13.09$ ,  $a_2 = 0.074$ ,  $a_3 = 0.007$  and  $a_4 = 11.89$  for the grain aspect ratio. Furthermore, for each of 14 specimen sets, the measured grain size ( $dxz$ ) and grain aspect ratios (GAR), as well as their calculated equivalents (Equation (11)), are collected in Table 3, along with the deviations between approximations and experiments.

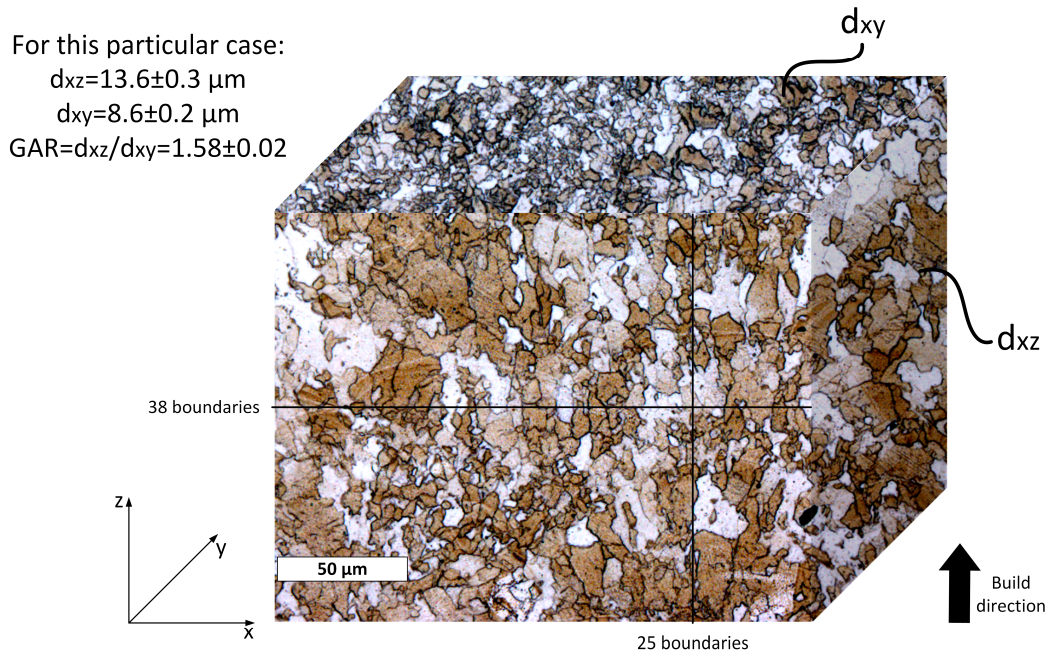


Figure 7. Metallography of Specimen 1 using a LEXT 4100 confocal microscope ( $\times 500$ ).

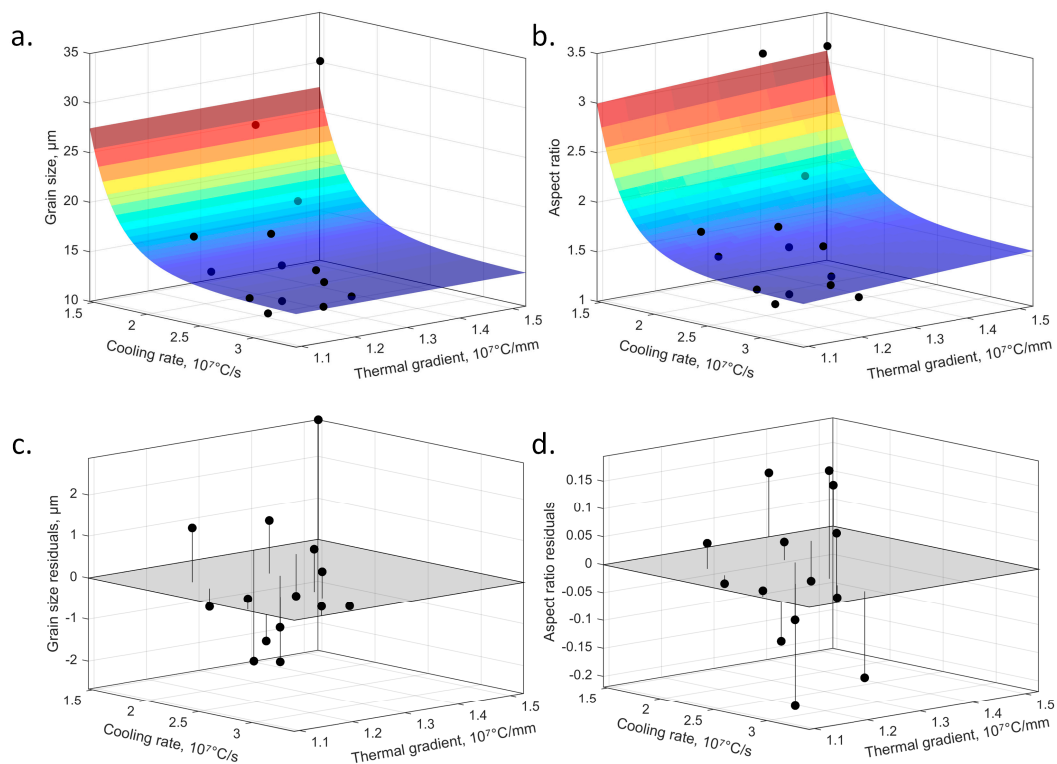


Figure 8. (a) Grain size ( $dxz$ ) and (b) grain aspect ratio (GAR) as functions of CR and TG; (c) Grain size and (d) grain aspect ratio residuals.

**Table 3.** Grain size (dxz) and grain aspect ratio (GAR) approximation-experiment comparison with deviations.

#	CR, 10 <sup>7</sup> °C/s	TG, 10 <sup>7</sup> °C/mm	Grain Size (dxz)			Grain Aspect Ratio (GAR)		
			Model, μm	Exp., μm	Dev., %	Model	Exp.	Dev., %
1	1.46	1.53	24.9	30.1 ± 0.9	17.3	2.9	3.2 ± 0.01	8.2
2	1.74	1.43	20.4	17.6 ± 1.0	13.7	2.3	2.0 ± 0.09	12.6
3	1.46	1.40	25	28.8 ± 1.4	0.8	2.9	3.2 ± 0.13	9.4
4	2.11	1.30	16.9	16.3 ± 1.1	3.6	1.9	1.7 ± 0.06	10.5
5	2.21	1.30	16.2	13.4 ± 1.1	17.3	1.8	1.5 ± 0.09	15.6
6	2.76	1.26	13.7	14.7 ± 1.5	6.8	1.4	1.7 ± 0.08	18.1
7	3.22	1.23	13.1	13.4 ± 2.8	2.2	1.4	1.3 ± 0.03	5.0
8	2.96	1.23	12.5	14.2 ± 2.3	12.0	1.3	1.5 ± 0.15	11.6
9	2.75	1.19	13.8	12.1 ± 0.6	12.3	1.4	1.3 ± 0.03	8.6
10	2.00	1.18	17.7	17.0 ± 2.5	4.0	2.0	1.8 ± 0.04	12.5
11	2.23	1.16	16.1	14.1 ± 1.0	12.4	1.8	1.6 ± 0.04	12.8
12	3.40	1.14	12.2	13.6 ± 2.0	10.3	1.2	1.6 ± 0.02	24.1
13	3.14	1.09	13.2	12.8 ± 1.8	3.0	1.4	1.4 ± 0.08	2.1
14	2.93	1.10	12.7	13.8 ± 0.8	8.0	1.3	1.5 ± 0.04	11.6

2.3. Grain Size (dxz) and Grain Aspect Ratio (GAR) Processing Maps

The analytical model of the melt pool (Equations (1)–(6)) and the approximation functions of Equation (11) can finally be combined to generate the grain size (dxz) and the grain aspect ratio (GAR) processing maps for iron powder (Figure 9a,b). These maps are calculated by varying the laser power from 20 to 380 W, the scanning speed from 100 to 4000 mm/s, and the hatching space from 60 to 90 μm, keeping the layer thickness constant at 40 μm.

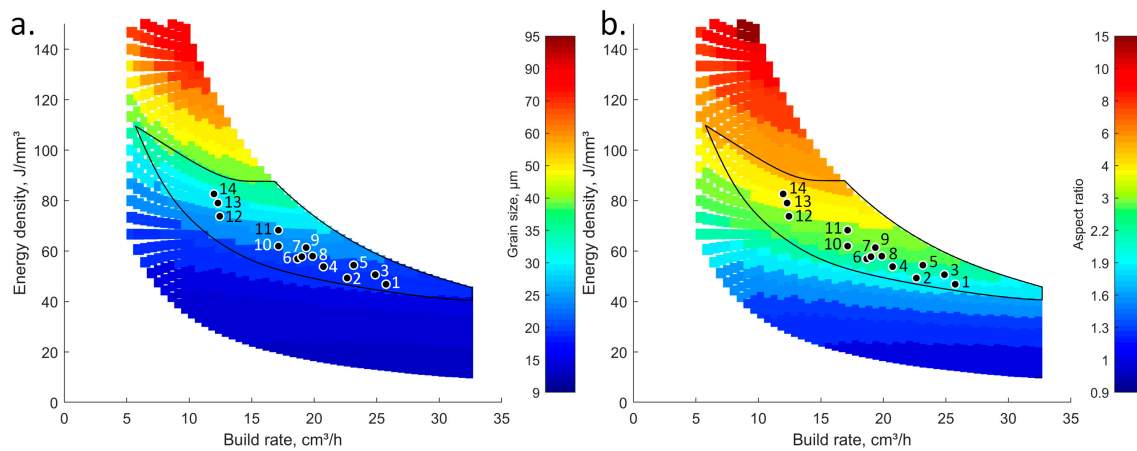


**Figure 9.** (a) Grain size (dxz) and (b) grain aspect ratio (GAR) processing maps for iron powder; contours delimit the processing conditions corresponding to a printed density  $\geq 99.9\%$ ; numbers from 1 to 14 identify processing conditions of the calibration specimens.

2.4. Validation Strategy and Results

At the beginning of this study, we hypothesized that the proposed grain size and grain aspect ratio prediction algorithm could be applied to other materials processed by an EOS M280 LPBF system. To verify the validity of this hypothesis, we selected another alloy, IN625, and carried out the validation in two stages. Firstly, the cooling rates calculated for LPBF of IN625 alloy were compared to their experimental equivalents taken from [24]. Secondly, the grain size and the grain aspect ratio calculated for the same alloy were compared with their experimental equivalents taken from [18]. (Note that the thermal gradient values were not experimentally available, thus limiting this validation to the CR values only).

For these validations studies, the CR,  $d_{xz}$  and GAR processing maps were calculated using the previously presented algorithm (Equations (1)–(6)), and the physical properties of IN625 bulk alloy and powder collected in Table 4 [27]. Note that for the first stage of validation (cooling rate), bulk material properties were used, since experimental data were obtained for a single laser melt track created on an IN625 plate. For the second validation stage, however (grain size and grain aspect ratio), powdered material properties were used, since the experimental data were obtained in the course of a conventional laser powder bed printing. In both cases, experimental data were obtained with similar EOS M270 and M280 LPBF systems to that used in this study. Note also that in this case, the powder bed density was set at 60% (approximated as a common value for gas- or plasma-atomized spherical powders).

**Table 4.** Physical properties of IN625 bulk and powdered alloy used for melt pool modeling [27,38].

	IN625	
	Bulk	Powder ( $t = 40 \mu\text{m}; \varphi = 60\%$ )
Liquidus temperature, °C	1350	1350
Solidus temperature, °C	1290	1290
Density, $\text{kg/m}^3$	8440	5064
Thermal conductivity, $\text{W/m} \times \text{K}$	25.2	12.6
Specific heat capacity, $\text{J/kg} \times \text{K}$	670	670
Electrical resistivity, $10^{-8} \Omega \times \text{m}$	134	622

### 3. Validation

#### 3.1. Cooling Rate Validation

To assess the validity of the cooling rate modeling, the numerical results are compared with experiment values obtained with laser power ranging from 150 to 195 W, and scanning speed from 400 to 1200 mm/s [24]. The calculated and experimental cooling rates are plotted in Figure 10a and summarized in Table 5, where the average deviation between the model and the experiment is 4.2%.

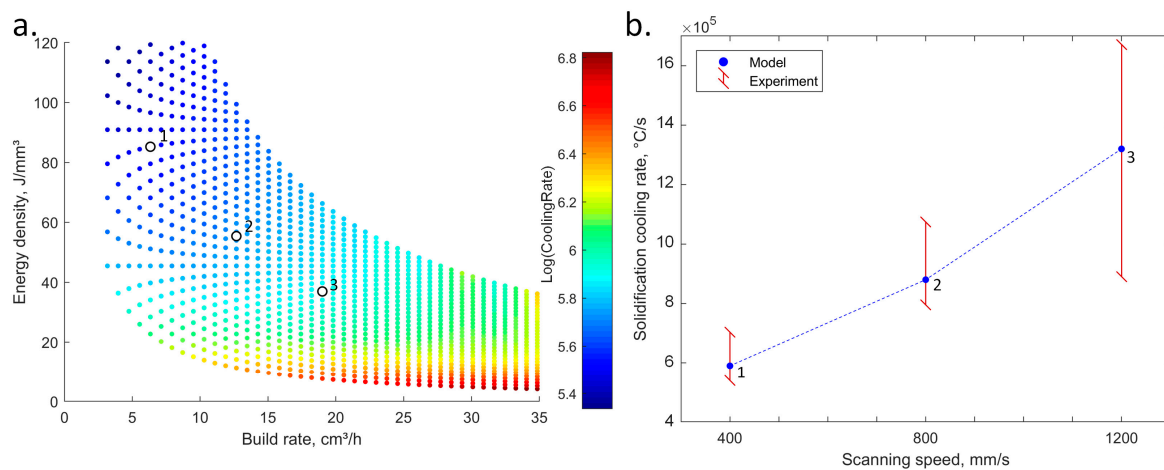


**Figure 10.** Comparison of the calculated and experimental CRs for IN625: (a) CR processing map; (b) scanning speed-CR plot; numbers 1 to 3 correspond to the three parameter sets presented in Table 5.

Table 5. Cooling rate model-experiment [24] comparison for IN625 alloy.

Case	Power, W	Speed, mm/s	Model	Cooling Rate, 10 <sup>5</sup> K/s	
				Experiment [24]	Deviation, %
1	150	400	5.97	6.20 ± 0.8	3.7
2	195	800	8.89	9.35 ± 1.4	4.9
3	195	1200	12.3	12.8 ± 3.9	3.9

Note that Figure 10b is plotted in the CR-scanning speed coordinates and not in the CR-BR coordinates, since experimental data were obtained for a single laser track on a solid building plate and therefore, neither the hatching space nor the layer thickness are relevant in this case.

### 3.2. Grain size and Grain Aspect Ratio Validation

The CR (Figure 11a) and GAR (Figure 11c) processing maps are now calculated using the melt pool model (Equations (1)–(6)), the physical properties of IN625 powder (Table 4), and the correspondence between the CR & TG and the grain size and the grain aspect ratio (Equation (11)). Then, the experimentally measured grain size and grain aspect ratio values [18] are superposed in Figure 11b,d, where deviations between the model and the experiment correspond to ~10% for the grain size and ~14% for the grain aspect ratio (see Table 6 for numerical values).

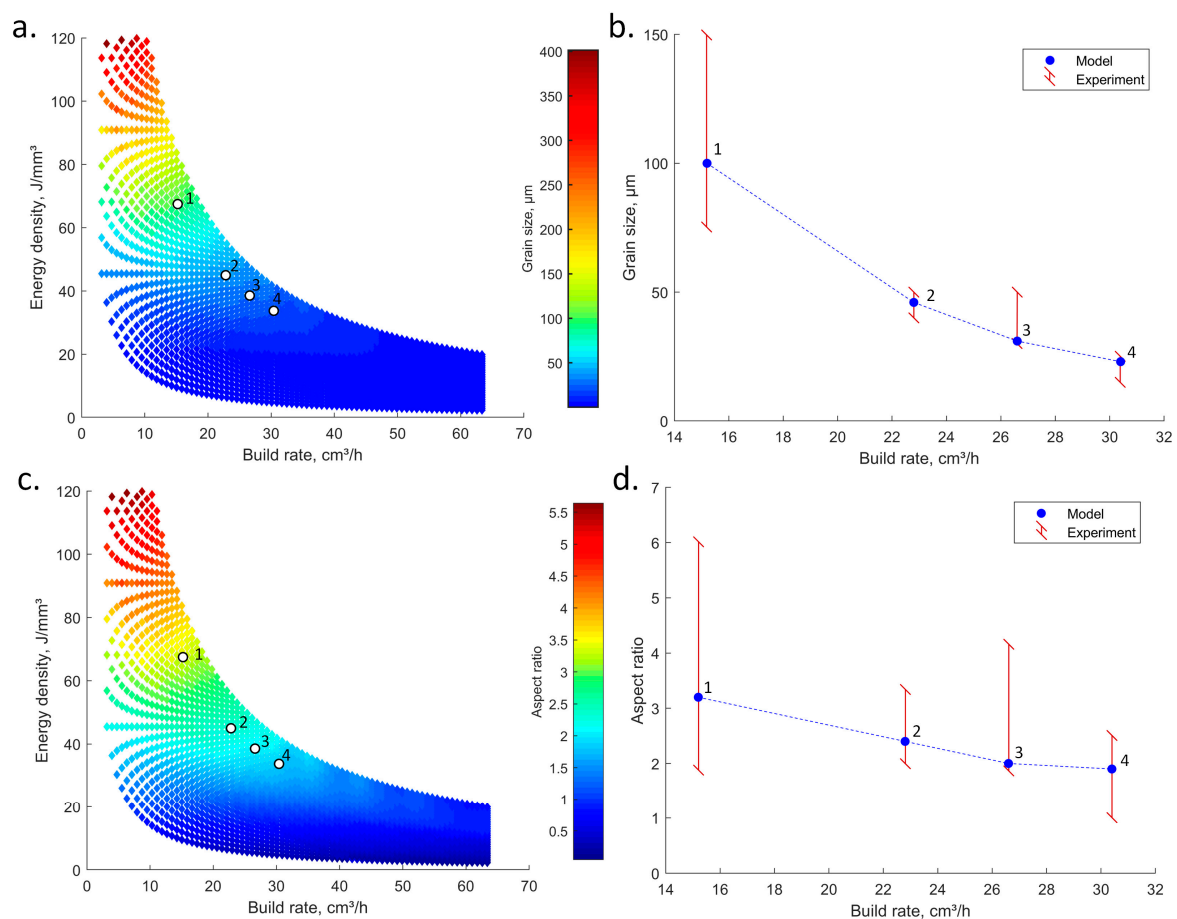


Figure 11. Grain size and grain aspect ratio validation: (a) Grain size (dxz) prediction map, (b) grain size: model versus experiment [18], (c) grain aspect ratio prediction map and (d) aspect ratio: model versus experiment; numbers 1 to 4 correspond to four parameter sets tested.

**Table 6.** Grain size (dxz) and grain aspect ratio ( $t = 40 \mu\text{m}$ ;  $h = 110 \mu\text{m}$ ): model versus experiment [18].

N°	P, W	V, mm/s	E, J/mm <sup>3</sup>	BR, cm <sup>3</sup> /h	Grain Size (dxz), $\mu\text{m}$			Aspect Ratio (AR)		
					Model, $\mu\text{m}$	Experim., $\mu\text{m}$	Dev., %	Model, $\mu\text{m}$	Experim., $\mu\text{m}$	Dev., %
1	285	960	67.5	15.2	100	100 <sup>+50</sup> <sub>-25</sub>	0	3.2	3.3 <sup>+2.7</sup> <sub>-1.4</sub>	5
2	285	1440	45.0	22.8	46	45 <sup>+5</sup> <sub>-5</sub>	2	2.4	2.5 <sup>+0.8</sup> <sub>-0.5</sub>	5
3	285	1680	38.5	26.6	31	35 <sup>+15</sup> <sub>-5</sub>	13	2.0	2.5 <sup>+1.7</sup> <sub>-0.6</sub>	19
4	285	1920	33.8	30.4	23	18 <sup>+7</sup> <sub>-3</sub>	27	1.9	1.5 <sup>+1</sup> <sub>-0.5</sub>	27

From this validation study, it appears that the average deviations between the model and the experimental data for Specimens 1 and 2 are quite low: 1% for the grain size and 5% for the grain aspect ratio, but for Specimens 3 and 4, these deviations increase to 13% for the grain size and to 27% for the grain aspect ratio. The latter discrepancies can be explained by the fact that the densities of Specimens 3 and 4 were lower than 99.9%, specifically, 99.1 and 97.3% [18]. The processing-induced porosity affected both the cooling rate and the thermal gradient, which was not taken into account by the model.

#### 4. Discussion

This study was conducted using a Gaussian heat source model for three main reasons:

- This model allows the simulation of thousands of printing parameter sets in a time-efficient way.
- It allows easy variations of the major LPBF input parameters.
- It had been successfully validated for iron [25], Ti-Zr-Nb [26] and IN625 [18] alloys in previous studies.

This model has been proven to be relevant and accurate for the grain size and aspect ratio predictions and constitutes a time-efficient solution for further process optimization in the field of additive manufacturing. It can also easily be used to get additional insight into other processing-induced issues that are strongly dependent on thermal exchanges, namely, the risks of hot cracking and distortions. Moreover, this model can be used for the creation of relevant diagrams, such as a Grain Growth Rate-Thermal Gradient diagram, similar to that used in welding [39] as shown in Figure 12.

Note, however, that the model of this study allows the prediction of an average grain size in the longitudinal plane of the LPBF processed alloys only. When the experimentally measured and calculated grain sizes are compared, the discrepancy between the results can be affected by the distance between the region of interest and the melt pool centerline. Moreover, pores induced by LPBF can suppress the epitaxial growth of grains, and therefore, areas adjacent to these pores can contain equiaxed grains, as shown in [18].

Furthermore, the approach used in the present work is based on grain growth under a sharp moving interface between liquid and solid states. A multi-scale approach involving dendrite growth, phase segregation and transformation phenomena represents a difficult numerical problem, and requires a phase field analysis based on the Gibbs free energy calculations, for example [40]. Thus, the use of this model for grain size prediction in the dual-phase ( $\alpha + \beta$ ) Ti-6Al-4V titanium alloy, or in steel with martensitic transformation cannot be recommended. However, the grain size and the grain aspect ratio in alloys with diffusion-dependent phase transformations (beta Ti alloys, austenitic stainless steel, ferritic steel, Nickel-based superalloys, Al alloys, etc.) are possible targets.

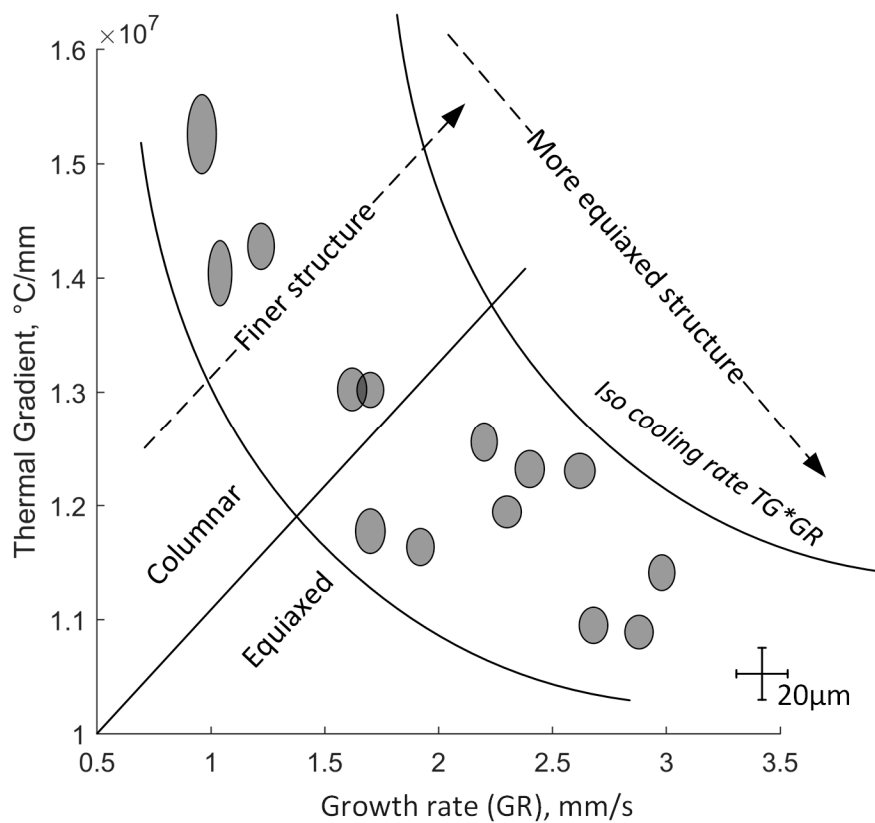


**Figure 12.** Grain morphology of LPBF iron as a function of the grain growth rate and the thermal gradient (idea of such a diagram is adopted from [39]).

*Additional Note*

In this study, the formation of the grain structure was considered for the case of a continuous single track built on a substrate with an initial temperature of 23 °C. However, due to the layer-by-layer and multiple pattern track strategies employed, the effective temperature of the substrate becomes higher than the initial temperature of 23 °C. To evaluate the influence of the multi-track phenomenon on the initial temperature of the substrate, let us consider a 10 mm-long laser track and a skywriting time of 0.50 ms, the latter corresponding to the time when the laser is switched off; both values are common values for LPBF systems (Figure 13).

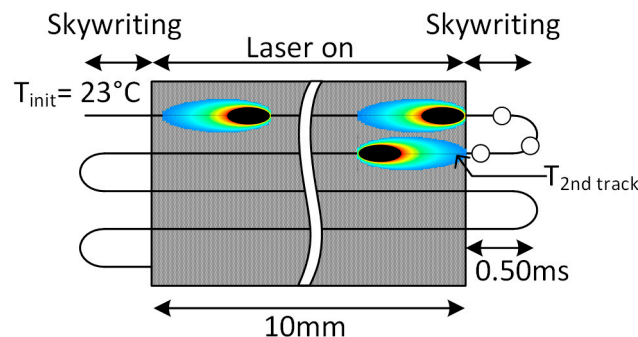


**Figure 13.** Schematic representation of the laser journey.

Given the preceding, the substrate temperature at the beginning of the next track can be evaluated by calculating the temperature at a one hatching space distance from the center of this track after a delay of 0.50 ms. For this study, depending on the processing conditions used to print 14 specimens (see Table 2), the substrate temperature ranges from 290 to 390 °C, which is very different from the 23 °C

used in our initial calculations. It is clear that the higher the initial temperature of the material prior to laser exposure, the smaller the cooling rate and temperature gradient, and consequently, the larger the grain size and the lower the grain aspect ratio. To assess the impact of this temperature increase on the deviations between the modeling and experimental results of this study, we recalculated the grain size and the grain aspect ratio of 14 specimens used for the model calibration (Figure 9), replacing the initial temperature of the powder bed of 23 °C with that calculated using the multi-track approach presented above.

As an example, the grain sizes (dxz) and the grain aspect ratios (GAR) predicted for Specimens 1 and 3 using the substrate temperatures of either 23 or 390 °C are compared with their experimental equivalents in Figure 14. The comparison shows that taking into account the temperature of the substrate improves the precision of both grain size and grain aspect ratio predictions. This confirms the possibility of using the simplified analytical model of this study for multi-track simulations, but additional effort needs to be deployed in order to obtain more reliable results. In fact, we only evaluated the influence of the temperature at the end of the part path. To develop a real multi-track model, this process should be replicated for every point along the laser journey.

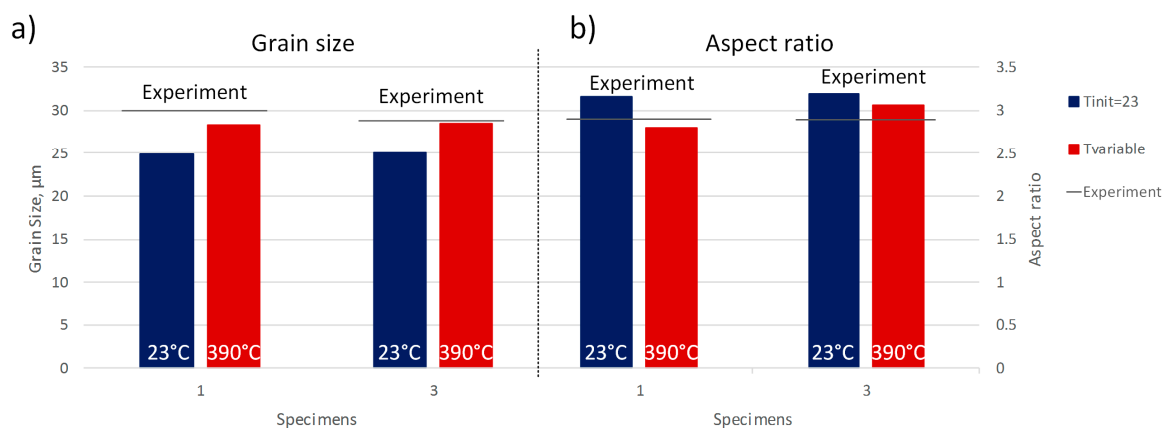


**Figure 14.** Grain size (a) and grain aspect ratio (b) predictions for Specimens 1 and 3 with variable initial substrate temperatures (23 °C blue, 390 °C red); average experimental data are presented by horizontal bars.

Finally, in order to evaluate the time efficiency of this approach, the cooling rate (CR) and the thermal gradient (TG) values were calculated using both the heat conduction model of this study and the concurrent thermal fluid model [24] for one set of LPBF parameters and  $1 \times 1 \times 1$  (mm<sup>3</sup>) volume space divided in  $10^6$  elements. To obtain the CR and TG values, the heat conduction model required 15 s per CPU, while the thermal fluid model required 100 s per CPU.

## 5. Conclusions

A simplified analytical model of the LPBF process was used to develop the grain size and aspect ratio prediction algorithm for a given powder feedstock and a given LPBF system. Using a set of microstructure calibration coupons built with the laser power varying from 255 to 350 W, the scanning speed from 1000 to 3000 m/s, and the hatching space from 60 to 90 µm, this model was adapted for a water-atomized iron powder and an M280 EOS LPBF system. The approach was then validated for different alloys and processing conditions using data from the literature, thus demonstrating that this model can be used for the LPBF process simulation. It was also shown that the hatching space and layer thickness values have a direct influence on the creation of the processing map, as previously demonstrated in [41–43], and must be taken into account during the calibration step. This step represents a must-follow requirement to improve the prediction capability of the model. This calibration step allows compensation for the fact that the model does not take into account the

specificities of a given LPBF system related to particular heat transfer and recoating conditions, which influence the final microstructure of manufactured parts. However, once calibrated for a selected LPBF system, the model could be used for different alloys processed with the same system to provide insights into the grain size and grain aspect ratio in the printed part.

**Author Contributions:** The work plan was developed by M.L. to meet the study objectives defined by himself and V.B. The specimen design and the alloy selection were carried out by all the coauthors based upon the state of the art, previous research by V.B. and A.K., and current trends in the field. The design, fabrication and testing of the specimens were performed by M.L.; V.B. contributed to the data organization, results interpretation and manuscript redaction. All authors have read and agreed to the published version of the manuscript.

**Funding:** This research was funded by NSERC (Natural Sciences and Engineering Research Council of Canada).

**Acknowledgments:** The authors would like to express their appreciation of the technical support provided by M. Samoilenko and V. Moudin.

**Conflicts of Interest:** The authors declare no conflicts of interest.

## References

1. ASTM International. *Standard Terminology for Additive Manufacturing Technologies*; ASTM International: Geauga County, OH, USA, 2012.
2. Sames, W.J.; List, F.A.; Pannala, S.; Dehoff, R.R.; Babu, S.S. The metallurgy and processing science of metal additive manufacturing. *Int. Mater. Rev.* **2016**, *61*, 315–360. [[CrossRef](#)]
3. Francois, M.M.; Sun, A.; King, W.E.; Henson, N.J.; Tourret, D.; Bronkhorst, C.A.; Carlson, N.N.; Newman, C.K.; Haut, T.S.; Bakosi, J.; et al. Modeling of additive manufacturing processes for metals: Challenges and opportunities. *Curr. Opin. Solid State Mater. Sci.* **2017**, *21*. [[CrossRef](#)]
4. Acharya, R.; Sharon, J.A.; Staroselsky, A. Prediction of microstructure in laser powder bed fusion process. *Acta Mater.* **2017**, *124*, 360–371. [[CrossRef](#)]
5. Price Waterhouse Coopers. *3D Printing and the New Shape of Industrial Manufacturing*; Pricewaterhouse Coopers LLP: London, UK, 2014.
6. Ghosh, S. Predictive modeling of solidification during laser additive manufacturing of nickel superalloys: Recent developments, future directions. *Mater. Res. Express* **2018**, *5*, 012001. [[CrossRef](#)]
7. Yadroitsau, I. Direct manufacturing of 3D objects by selective laser melting of metal powders. Ph.D. Thesis, ENISE, Saint-Etienne, France, 2008.
8. Khairallah, S.A.; Anderson, A.T.; Rubenchik, A.; King, W.E. Laser powder-bed fusion additive manufacturing: Physics of complex melt flow and formation mechanisms of pores, spatter, and denudation zones. *Acta Mater.* **2016**, *108*, 36–45. [[CrossRef](#)]
9. King, W.E.; Barth, H.D.; Castillo, V.M.; Gallegos, G.F.; Gibbs, J.W.; Hahn, D.E.; Rubenchik, A.M. Observation of keyhole-mode laser melting in laser powder-bed fusion additive manufacturing. *J. Mater. Process. Technol.* **2014**, *214*, 2915–2925. [[CrossRef](#)]
10. King, W.E.; Barth, H.D.; Castillo, V.M.; Gallegos, G.F.; Gibbs, J.W.; Hahn, D.E.; Kamath, C.; Rubenchik, A.M. Laser powder bed fusion additive manufacturing of metals; physics, computational, and materials challenges. *Appl. Phys. Rev.* **2015**, *2*, 041304. [[CrossRef](#)]
11. Farzadi, A.; Do-Quang, M.; Kokabi, A.H.; Serajzadeh, S. Phase-field simulation of weld solidification microstructure in an Al–Cu alloy. *Model. Simul. Mater. Sci. Eng.* **2008**, *16*, 065005. [[CrossRef](#)]
12. Johnson, L.; Mahmoudi, M.; Zhang, B.; Seede, R.; Huang, X.; Maier, J.T.; Maier, H.J.; Karaman, I.; Elwany, A.; Arróyave, R. Assessing printability maps in additive manufacturing of metal alloys. *Acta Mater.* **2019**, *176*, 199–210. [[CrossRef](#)]
13. Boettinger, W.J.; Warren, J.A.; Beckermann, C.; Karma, A. Phase-field simulation of solidification. *Annu. Rev. Mater. Res.* **2002**, *32*, 163–194. [[CrossRef](#)]
14. Chen, L.-Q. Phase-field models for microstructure evolution. *Annu. Rev. Mater. Res.* **2002**, *32*, 113–140. [[CrossRef](#)]
15. Steinbach, I. Phase-field models in materials science. *Model. Simul. Mater. Sci. Eng.* **2009**, *17*, 073001. [[CrossRef](#)]
16. Kundin, J.; Mushongera, L.; Emmerich, H. Phase-field modeling of microstructure formation during rapid solidification in Inconel 718 superalloy. *Acta Mater.* **2015**, *95*, 343–356. [[CrossRef](#)]

17. Rodgers, T.M.; Madison, J.D.; Tikare, V. Simulation of metal additive manufacturing microstructures using kinetic Monte Carlo. *Comput. Mater. Sci.* **2017**, *135*, 78–89. [[CrossRef](#)]
18. Poulin, J.-R.; Kreitchberg, A.; Terriault, P.; Brailovski, V. Long fatigue crack propagation behavior of laser powder bed-fused inconel 625 with intentionally-seeded porosity. *Int. J. Fatigue* **2019**, *127*, 144–156. [[CrossRef](#)]
19. Bhutto, A.; Wahab, M.S.; Raus, A.A.; Kamarudin, K. Effects of Selective Laser Melting Parameters on Relative Density of AlSi10Mg. *Int. J. Eng. Technol.* **2016**, *8*, 2552–2557.
20. Krishnan, M.; Atzeni, E.; Canali, R.; Calignano, F.; Ambrosio, E.P.; Iuliano, L. On the effect of process parameters on properties of AlSi10Mg parts produced by DMLS. *Rapid Prototyp. J.* **2014**, *20*, 449–458. [[CrossRef](#)]
21. Ghosh, S.; Ma, L.; Ofori-Opoku, N.; Guyer, J.E. On the primary spacing and microsegregation of cellular dendrites in laser deposited Ni-Nb alloys. *Model. Simul. Mater. Sci. Eng.* **2017**, *25*, 065002. [[CrossRef](#)]
22. Panwisawas, C.; Qiu, C.; Anderson, M.J.; Sovani, Y.; Turner, R.P.; Attallah, M.M.; Basoalto, H.C. Mesoscale modelling of selective laser melting: Thermal fluid dynamics and microstructural evolution. *Comput. Mater. Sci.* **2017**, *126*, 479–490. [[CrossRef](#)]
23. Lee, Y.; Zhang, W. Modeling of heat transfer, fluid flow and solidification microstructure of nickel-base superalloy fabricated by laser powder bed fusion. *Addit. Manuf.* **2016**, *12*, 178–188. [[CrossRef](#)]
24. Gan, Z.; Lian, Y.; Lin, S.E.; Jones, K.K.; Kam Liu, W.; Wagner, G.J. Benchmark Study of Thermal Behavior, Surface Topography, and Dendritic Microstructure in Selective Laser Melting of Inconel 625. *Integr. Mater. Manuf. Innov.* **2019**, *8*, 178–193. [[CrossRef](#)]
25. Letenneur, M.; Brailovski, V.; Kreitchberg, A.; Paserin, V.; Bailon-Poujol, I. Laser powder bed fusion of water-atomized iron-based powders: Process optimization. *J. Manuf. Mater. Process.* **2017**, *1*, 23. [[CrossRef](#)]
26. Kreitchberg, A.; Brailovski, V.; Prokoshkin, S. New biocompatible near-beta Ti-Zr-Nb alloy processed by laser powder bed fusion: Process optimization. *J. Mater. Process. Technol.* **2018**, *252*, 821–829. [[CrossRef](#)]
27. Letenneur, M.; Brailovski, V.; Kreitchberg, A. Optimization of Laser Powder Bed Fusion Processing Using a Combination of Melt Pool Modeling and Design of Experiment Approaches: Density Control. *J. Manuf. Mater. Process.* **2019**, *3*, 21. [[CrossRef](#)]
28. Nie, P.; Ojo, O.; Li, Z. Numerical modeling of microstructure evolution during laser additive manufacturing of a nickel-based superalloy. *Acta Mater.* **2014**, *77*, 85–95. [[CrossRef](#)]
29. Schuöcker, D. *Handbook of the Eurolaser Academy*; Springer Science & Business Media: Berlin, Germany, 1998; Volume 2.
30. Hagen, E.; Rubens, H. Über Beziehungen des Reflexions-und Emissionsvermögens der Metalle zu ihrem elektrischen Leitvermögen. *Annalen der Physik* **1903**, *316*, 873–901. [[CrossRef](#)]
31. Liepa, T. AMB2018-02 Description. 2018. Available online: <https://www.nist.gov/ambench/amb2018-02-description> (accessed on 13 September 2019).
32. Bala, K.; Pradhan, P.R.; Saxena, N.S.; Saksena, M.P. Effective thermal conductivity of copper powders. *J. Phys. D: Appl. Phys.* **1989**, *22*, 1068. [[CrossRef](#)]
33. Liu, P.; Fu, C.; Li, T. Calculation formula for apparent electrical resistivity of high porosity metal materials. *Sci. China Ser. E Technol. Sci.* **1999**, *42*, 294–301. [[CrossRef](#)]
34. Jacob, G.; Donmez, A.; Slotwinski, J.; Moylan, S. Measurement of powder bed density in powder bed fusion additive manufacturing processes. *Meas. Sci. Technol.* **2016**, *27*, 115601. [[CrossRef](#)]
35. Valencia, J.J.; Quedsted, P.N. Thermophysical Properties. In *CASTING*; Viswanathan, S., Ed.; ASM International: Geauga County, OH, USA, 2008.
36. Powell, R.; Ho, C.Y.; Liley, P.E. *Thermal Conductivity of Selected Materials*; National Bureau of Standards Washington, US Department of Commerce: Gaithersburg, MD, USA, 1966; Volume 8.
37. ASTM International. *E112-13 Standard Test Methods for Determining Average Grain Size*; ASTM International: West Conshohocken, PA, USA, 2013.
38. Mankins, W.L.; Lamb, S. Nickel and Nickel Alloys. In *Properties and Selection: Nonferrous Alloys and Special-Purpose Materials*; ASM International: Geauga County, OH, USA, 1990.
39. Kou, S. *Welding Metallurgy*; John Wiley & Sons, Inc.: Hoboken, NJ, USA, 2003; pp. 431–446.
40. Cool, T.; Bartol, A.; Kasenga, M.; Modi, K.; García, R.E. Gibbs: Phase equilibria and symbolic computation of thermodynamic properties. *Calphad* **2010**, *34*, 393–404. [[CrossRef](#)]
41. Sufiiarov, V.S.; Popovich, A.A.; Borisov, E.V.; Polozov, I.A.; Masaylo, D.V.; Orlov, A.V. The effect of layer thickness at selective laser melting. *Procedia Eng.* **2017**, *174*, 126–134. [[CrossRef](#)]

42. Liverani, E.; Toschi, S.; Ceschini, L.; Fortunato, A. Effect of selective laser melting (SLM) process parameters on microstructure and mechanical properties of 316L austenitic stainless steel. *J. Mater. Process. Technol.* **2017**, *249*, 255–263. [[CrossRef](#)]
43. Kreitchberg, A.; Brailovski, V.; Sheremetyev, V.; Prokoshkin, S. Effect of laser powder bed fusion parameters on the microstructure and texture development in superelastic Ti–18Zr–14Nb alloy. *Shape Mem. Superelasticity* **2017**, *3*, 361–372. [[CrossRef](#)]



© 2020 by the authors. Licensee MDPI, Basel, Switzerland. This article is an open access article distributed under the terms and conditions of the Creative Commons Attribution (CC BY) license (<http://creativecommons.org/licenses/by/4.0/>).